Cellular/Molecular

Nonlinear Relationship Between Spike-Dependent Calcium Influx and TRPC Channel Activation Enables Robust Persistent Spiking in Neurons of the Anterior Cingulate Cortex

Stéphanie Ratté,[1,2,3] Sergei Karnup,[3] and Steven A. Prescott[1,2,3]

[1]Neurosciences and Mental Health, The Hospital for Sick Children, Toronto, Ontario, M5G 0A4 Canada, [2]Department of Physiology and the Institute of Biomaterials and Biomedical Engineering, University of Toronto, Toronto, Ontario, M5S 1A8 Canada, and [3]Pittsburgh Center for Pain Research, University of Pittsburgh, Pittsburgh, Pennsylvania, 15213

Continuation of spiking after a stimulus ends (i.e. persistent spiking) is thought to support working memory. Muscarinic receptor activation enables persistent spiking among synaptically isolated pyramidal neurons in anterior cingulate cortex (ACC), but a detailed characterization of that spiking is lacking and the underlying mechanisms remain unclear. Here, we show that the rate of persistent spiking in ACC neurons is insensitive to the intensity and number of triggers, but can be modulated by injected current, and that persistent spiking can resume after several seconds of hyperpolarization-imposed quiescence. Using electrophysiology and calcium imaging in brain slices from male rats, we determined that canonical transient receptor potential (TRPC) channels are necessary for persistent spiking and that TRPC-activating calcium enters in a spike-dependent manner via voltage-gated calcium channels. Constrained by these biophysical details, we built a computational model that reproduced the observed pattern of persistent spiking. Nonlinear dynamical analysis of that model revealed that TRPC channels become fully activated by the small rise in intracellular calcium caused by evoked spikes. Calcium continues to rise during persistent spiking, but because TRPC channel activation saturates, firing rate stabilizes. By calcium rising higher than required for maximal TRPC channel activation, TRPC channels are able to remain active during periods of hyperpolarization-imposed quiescence (until calcium drops below saturating levels) such that persistent spiking can resume when hyperpolarization is discontinued. Our results thus reveal that the robust intrinsic bistability exhibited by ACC neurons emerges from the nonlinear positive feedback relationship between spike-dependent calcium influx and TRPC channel activation.

Key words: anterior cingulate cortex; bistability; calcium; persistent spiking; TRPC channels; working memory

Significance Statement

Neurons use action potentials, or spikes, to encode information. Some neurons can store information for short periods (seconds to minutes) by continuing to spike after a stimulus ends, thus enabling working memory. This so-called "persistent" spiking occurs in many brain areas and has been linked to activation of canonical transient receptor potential (TRPC) channels. However, TRPC activation alone is insufficient to explain many aspects of persistent spiking such as resumption of spiking after periods of imposed quiescence. Using experiments and simulations, we show that calcium influx caused by spiking is necessary and sufficient to activate TRPC channels and that the ensuing positive feedback interaction between intracellular calcium and TRPC channel activation can account for many hitherto unexplained aspects of persistent spiking.

Introduction

Continuing to spike after stimulation ends is an important way by which neurons store information on a timescale of seconds to minutes (Fuster and Alexander, 1971). This persistent spiking is thus thought to underpin working memory (Durstewitz et al., 2000; Brody et al., 2003; Hasselmo and Stern, 2006). Cholinergic modulation in brain areas such as medial prefrontal cortex (PFC), including the anterior cingulate cortex (ACC), is also

Received Feb. 23, 2017; revised Dec. 18, 2017; accepted Jan. 8, 2018.

Author contributions: S.A.P. designed research; S.R., S.K., and S.A.P. performed research; S.R., S.K., and S.A.P. analyzed data; S.R., S.K., and S.A.P. wrote the paper.

This work was supported by the National Institute of Neurological Disorders and Stroke–National Institutes of Health (Grant R01-NS076706) and the Natural Sciences and Engineering Research Council (Discovery Grant to S.A.P.). S.A.P. was also supported by a Scholar Award from the Edward Mallinckrodt, Jr. Foundation, a Canadian Institutes of Health Research New Instigator Award, and an Ontario Early Researcher Award.

The authors declare no competing financial interests.

Correspondence should be addressed to Steven A. Prescott, Neurosciences and Mental Health, The Hospital for Sick Children, 686 Bay St., Toronto, ON, M5G 0A4 Canada. E-mail: steve.prescott@sickkids.ca.

DOI:10.1523/JNEUROSCI.0538-17.2018

 0270-6474/18/381788-14$15.00/0

known to be crucial for working memory (Broersen et al., 1995). It is therefore notable that muscarinic receptor activation enables persistent spiking in ACC neurons (Haj-Dahmane and Andrade, 1996; Zhang and Séguéla, 2010) and in neurons of the hippocampus (Fraser and MacVicar, 1996; Knauer et al., 2013), amygdala (Egorov et al., 2006), entorhinal cortex (Egorov et al., 2002), perirhinal cortex (Navaroli et al., 2012), and primary somatosensory, visual, and motor cortices (Rahman and Berger, 2011). Evidence that muscarinic receptors in PFC are downregulated in a rat model of neuropathic pain and that this compromises persistent spiking (Radzicki et al., 2017) is interesting given that working memory is impaired in chronic pain patients (Berryman et al., 2013). Muscarinic receptor blockade in PFC is also known to compromise working memory (Major et al., 2015).

Persistent spiking can be supported by recurrent synaptic connections or, as in the examples listed above, by individual neurons that are intrinsically bistable (Durstewitz et al., 2000; Zylberberg and Strowbridge, 2017). Intrinsic bistability has been linked to the calcium-activated, nonspecific cation current (I_{CAN}), which has in turn been linked to canonical transient receptor potential (TRPC) channels, especially TRPC5 (Reboreda et al., 2011). Muscarinic receptor activation leads to rapid translocation of TRPC5 channels to the cell surface (Tai et al., 2011) whereupon they are gated by increases in intracellular calcium. Sensitivity of persistent spiking to nifedipine (Egorov et al., 2002; Zhang and Séguéla, 2010; Rahman and Berger, 2011) argues that L-type voltage-gated calcium channels (VGCCs) provide the necessary calcium. Blockade of persistent spiking by BAPTA, but not by EGTA, argues (based on faster calcium buffering by BAPTA) that VGCCs and TRPC channels operate in close spatial proximity (Blair et al., 2009; Gross et al., 2009; Rahman and Berger, 2011). The inward current carried by TRPC channels leads to a positive feedback loop, which, via elevation of intracellular calcium as an intermediary, yields persistent spiking.

Despite these and other biophysical details having been worked out (see Discussion), many aspects of persistent spiking remain difficult to explain. For instance, persistent spiking is graded (i.e., sensitive to the number and/or intensity of triggers) in some neurons, such as in entorhinal cortex (Egorov et al., 2002), but not in others, as shown here for ACC. The dynamical explanation for graded persistent spiking necessitates a line attractor or moveable fixed-point attractor (Brody et al., 2003; Fransen et al., 2006), whereas nongraded spiking can be accounted for by a simpler bistable system. However, other features of persistent spiking must also be explained. For instance, persistent spiking can resume after a period of quiescence (Durstewitz et al., 2000), but this so-called robustness to distractors must be achieved without making persistent spiking difficult to trigger. This implies an asymmetric relationship between the two attractors and the threshold that separates them; in other words, the spiking attractor must be farther from threshold than the quiescent attractor is from threshold. Furthermore, firing rate can vary during persistent spiking (Brody et al., 2003; Durstewitz and Seamans, 2006), which implies that the spiking attractor does not restrict spiking to a certain rate. These features affect how persistent spiking supports working memory. A deeper mechanistic understanding of persistent spiking at the cellular level would facilitate efforts to understand and manipulate working memory.

By combining electrophysiology and calcium imaging in rat brain slices with computational modeling and nonlinear dynamical analysis, we show here that these subtle yet functionally important aspects of persistent spiking in ACC neurons emerge from the nonlinear relationship between intracellular calcium and TRPC channel activation.

Materials and Methods

Experiments

All procedures were approved by the Institutional Animal Care and Use Committee at the University of Pittsburgh and the Animal Care Committee at The Hospital for Sick Children. Male Sprague Dawley rats 30–60 d old were anesthetized with isoflurane and decapitated. The brain was rapidly removed and immersed in ice-cold artificial CSF (aCSF) composed of the following (in mM): 124 NaCl, 26 $NaHCO_3$, 3 KCl, 1.25 NaH_2PO_4, 2 $MgCl_2$, 2 $CaCl_2$, and 10 glucose and bubbled with 95% O_2 and 5% CO_2. Using a Leica VT-1000S microtome, coronal slices (400 μm thick) were prepared from cortex rostral to bregma. Slices were kept at room temperature until recording, when they were transferred to a recording chamber perfused at 2 ml/min with carbogenated aCSF at room temperature. In a subset of experiments identified in the Results, testing was repeated at a bath temperature of 31°C. The perfusing aCSF also included 10 μM CNQX (Tocris Bioscience), 40 μM D-AP-5 (Ascent Scientific), and 10 μM bicuculline (Abcam) to block synaptic transmission. Based on past studies (Fransen et al., 2006; Zhang and Séguéla, 2010), 10 μM carbachol (CCh; Acros) was added to the bath after patching; other concentrations were not tested. SKF-96365 (Tocris Bioscience), flufenamic acid (Abcam), tetrodotoxin (Abcam), and thapsigargin (Tocris Bioscience) were added as reported in Results.

Electrophysiology. Patch pipettes were pulled from borosilicate glass capillaries (World Precision Instruments) on a P-97 puller (Sutter Instruments). For whole-cell recordings, the pipette solution contained the following (in mM): 144 K-gluconate, 2 NaCl, 2 $MgCl_2$, 10 HEPES, 0.2 EGTA, 3 Mg_2ATP, and 0.3 Na_2GTP; pH was adjusted to 7.3 with KOH and final osmolality was 285 mOsm. Other components were added to the pipette solution for calcium imaging and buffering experiments, as explained below. Only recordings with an access resistance <20 MΩ and a regular spiking pattern were included. For perforated patch recordings, Amphotericin-B (400 μg/ml; Sigma-Aldrich) and 0.1% Lucifer yellow was added to the pipette solution. Procedures described by Linley (2013) were followed. Lack of intracellular labeling with Lucifer yellow was confirmed at the end of recording. Neurons in Brodmann area 24 (Vogt and Paxinos, 2014) were visualized with gradient contrast optics and were recorded from in whole-cell configuration using an Axopatch-200B amplifier (Molecular Devices). Responses were low-pass filtered at 2 kHz and digitized at 20 kHz using a Power1401 computer interface and Signal5 software (Cambridge Electronic Design).

Dynamic clamp. Using the dynamic-clamp capabilities of Signal5, we implemented a virtual CAN current with a reversal potential of 0 mV and steady-state activation described by the following:

$$\frac{g}{g_{max}} = z_\infty(V) = \left[1 + e^{-\frac{V - V_{half}}{V_{slope}}}\right]^{-1} \quad (1)$$

$$\frac{dz}{dt} = \frac{z_\infty(V) - z}{\tau_z} \quad (2)$$

which means the gating variable z has steep-voltage dependence ($V_{slope} = 5$ mV) with half-maximal activation (V_{half}) at 0 mV, so that the virtual CAN current is activated only during spikes. $\tau_z = 2$ s, which is consistent with the rate of calcium clearance used in our computational model (see below). Calcium-dependent activation was not modeled because calcium concentration could not be measured in real time. The virtual CAN current was applied through the recording pipette to the soma, which is consistent with the somatic localization of TRPC channels (von Bohlen Und Halbach et al., 2005).

Calcium imaging. In one set of imaging experiments, Calcium Green-1 hexapotassium salt (100 μM; Invitrogen) was included in the intracellular recording solution. After diffusion of indicator throughout the cytosol, changes in intracellular calcium levels were imaged using a NeuroCCD-SM256 imaging system (RedShirt) mounted on a Zeiss AxioExaminer microscope equipped with a 40× objective. Excitation light was provided by an Xcite 200 DC light source (Lumen Dynamics) using a BP 500/25 nm excitation filter and emitted light was detected by the CCD camera via a BP 535/30 nm emission filter (Zeiss filter set 46HE). The full-frame image acquisition rate was 25 Hz and was synced to the electrophysio-

logical data acquisition via digital triggers. Images were analyzed using Neuroplex software (RedShirt). In separate experiments, Fluo-4 or Fluo-5F pentapotassium salt (100 μM; Life Technologies) was used instead of Calcium Green-1 and was imaged by two-photon microscopy using a VIVO 2-photon system (3i) with the Ti:Sapphire Laser (Chameleon Ultra II; Coherent) set to 800 nm. The reduced phototoxicity and bleaching associated with two-photon microscopy allowed for collection of longer datasets from which to measure calcium clearance kinetics. Moreover, the lower-affinity of Fluo-4 and Fluo-5F compared with Calcium Green-1 is preferable for measuring calcium kinetics (Grienberger and Konnerth, 2012).

Intracellular calcium buffering. A 2 mM diazo-2 tetrapotassium salt (Invitrogen) was added to the pipette solution. Formed by addition of a diazoacetyl group to one of the benzene rings in BAPTA, diazo-2 increases its calcium affinity by ~30 fold (K_d shifts from 2.2 μM to 73 nM) upon photoactivation by UV light (Adams et al., 1989). In the absence of a flash lamp, we activated diazo-2 using a metal halide lamp (XCite 200 DC; Lumen Dynamics) passed through a G365 excitation filter (Zeiss filter set 2) for 1–5 s (Zucker, 2010) controlled with a SmartShutter (Sutter Instruments) synced to the acquisition software.

Experimental design and statistical analyses. Data were analyzed using SigmaPlot11 (Systat) and are reported as mean ± SEM. Kolmogorov–Smirnov tests were used to verify that distributions were Gaussian. Paired or unpaired *t* tests were applied as appropriate. All tests are identified in the Results.

Computational modeling and analysis

Starting from a modified Morris–Lecar model described previously by us (Prescott et al., 2006), we added a calcium current and calcium-activated non-specific cation current to give the following:

$$C\frac{dV}{dt} = I_{stim} - g_{leak} \cdot (V - E_{leak}) - \bar{g}_{Na} \cdot m_\infty(V) \cdot (V - E_{Na}) - \bar{g}_K \cdot w \cdot (V - E_K) - \bar{g}_{fAHP} \cdot a_f \cdot (V - E_K) - \bar{g}_{sAHP} \cdot a_s \cdot (V - E_K) - \bar{g}_{Ca} \cdot b \cdot (V - E_{Ca}) - \bar{g}_{CAN} \cdot z_\infty(Ca) \cdot (V - E_{cation}) \quad (3)$$

$$\frac{dw}{dt} = \phi \cdot \frac{w_\infty(V) - w}{\tau_w(V)} \quad (4)$$

$$m_\infty(V) = \frac{1}{2} \cdot \left[1 + \tanh\left(\frac{V - \beta_m}{\gamma_m}\right)\right] \quad (5)$$

$$w_\infty(V) = \frac{1}{2} \cdot \left[1 + \tanh\left(\frac{V - \beta_w}{\gamma_w}\right)\right] \quad (6)$$

$$\tau_w(V) = \frac{1}{\cosh\left(\frac{V - \beta_w}{2\gamma_w}\right)} \quad (7)$$

$$x_\infty(V) = \left[1 + e^{-\frac{V - V_{half}}{V_{slope}}}\right]^{-1} \quad (8)$$

$$\frac{dx}{dt} = \frac{x_\infty(V) - x}{\tau_x} \quad (9)$$

where V is voltage and m, w, a_f, a_s, b, and z are gating variables Gating variables m and z activate quickly upon changes in V and Ca^{2+}, respectively, and were therefore modeled as instantaneously reaching steady state. In Equations 8 and 9, x corresponds to a_f, a_s, or b. The following parameters were used in all simulations: $C = 2$ μF/cm^2, $\phi = 0.15$, $E_{leak} = -70$ mV, $E_{Na} = 50$ mV, $E_K = -90$ mV, $E_{Ca} = 100$ mV, $E_{CAN} = 0$ mV, $\beta_m = -1.2$ mV, $\gamma_m = 18$ mV, $\beta_w = 0$ mV, $\gamma_w = 10$ mV, $\tau_{af} = 200$ ms, $\tau_{af} = 2$ s, and $\tau_b = 1$ ms. The gating variable z depends on intracellular calcium, as explained below. Conductance densities were (in mS/cm^2): leak conductance $g_{leak} = 2$, fast sodium conductance $\bar{g}_{Na} = 20$, delayed rectifier potassium conductance $\bar{g}_K = 20$, fast AHP conductance $\bar{g}_{fAHP} = 50$, slow AHP conductance $\bar{g}_{sAHP} = 25$, high-voltage activated calcium conductance $\bar{g}_{Ca} = 0.005$, and calcium-activated nonspecific cation (TRPC) conductance $\bar{g}_{CAN}$ was varied. Both AHP currents and the calcium current have steep voltage-dependent activation curves centered at 0 mV ($V_{slope} = 5$ mV; $V_{half} = 0$ mV) so that they are only activated during spikes (cf. Eqs. 8 and 9 with Eqs. 1 and 2); the AHP currents are in reality activated by spike-dependent calcium influx, but their coupling to suprathreshold voltage accurately recapitulated spike rate adaptation (Prescott and Sejnowski, 2008) and facilitated bifurcation analysis insofar as the effects of systematically varying calcium were linked exclusively to TRPC channels by avoiding confounding effects of altered spike rate adaptation. Intracellular calcium concentration $[Ca^{2+}]_i$ (in μM) depends on influx through voltage-gated calcium channels and clearance via a simple decay process as follows:

$$\frac{dCa^{2+}}{dt} = SAV \cdot \frac{\bar{g}_{Ca} \cdot b \cdot (V - E_{Ca})}{F} - \frac{Ca^{2+}}{\tau_{ca}} \quad (10)$$

where $\tau_{Ca} = 2$ s (Abel et al., 2004), F is the Faraday constant, surface area-to-volume ratio $SAV = s/r$ with shape $s = 3$ for a spherical soma and radius $r = 10$ μm; a scaling factor of 10^{-4} must be applied to SAV for the desired unit, cm^{-1} (Ratté and Prescott, 2011). Subsequent experiments revealed that τ_{Ca} was ~3.4 s, but test simulations using this slightly slower rate did not reveal qualitative differences from original simulations using $\tau_{Ca} = 2$ s. Calcium sensitivity of g_{CAN} was modeled as follows:

$$z_\infty(Ca^{2+}) = \left[1 + e^{-\frac{Ca - Ca_{half}}{Ca_{slope}}}\right]^{-1} \quad (11)$$

where $Ca_{half} = 0.4$ μM and $Ca_{slope} = 0.2$ μM (Strübing et al., 2001; Blair et al., 2009; Gross et al., 2009). Very similar results were obtained for a range of parameter values, or when g_{CAN} activation was modeled as a Hill function. In particular, we repeated several simulations with $Ca_{half} = 0.5$ μM and resting $[Ca^{2+}]_i = 0.1$ μM (instead of 0 μM, as per Eq. 10) and obtained nearly identical results to those reported. According to Blair et al. (2009), TRPC channels are partially activated at resting calcium levels and are maximally activated at ~1 μM calcium, which is what we have modeled here. Buffering experiments suggest that calcium microdomains exist (see Introduction), but they were not modeled here. ACC neurons most likely express TRPC1/5 heteromers (see Discussion), which have been reported to display a negative slope in their *I–V* curve at voltages below −40 mV (Strübing et al., 2001), which is consistent with Haj-Dahmane and Andrade (1999), but other studies showed a less pronounced bend in the *I–V* curve (Alfonso et al., 2008; Rubaiy et al., 2017). Because experimentally measured voltages during the interspike interval remained quite depolarized, even during hyperpolarizing steps, TRPC voltage sensitivity was not included in the model.

Equations were numerically integrated in XPP (Ermentrout, 2002) using the Runge–Kutta method with a 0.1 ms time step. Bifurcation analysis was conducted in AUTO using the XPP interface. All computer code will be made available at prescottlab.ca.

Results

Properties of persistent spiking in ACC pyramidal neurons

Persistent spiking was never observed in ACC pyramidal neurons tested in standard aCSF, whereas after the addition of 10 μM CCh to activate muscarinic acetylcholine receptors, brief suprathreshold depolarization triggered persistent spiking in 43 of 78 layer II/III pyramidal neurons and 55 of 94 layer V pyramidal neurons. Figure 1*A* shows a typical example of persistent spiking and the response in the same cell to the same stimulus before CCh. Neurons with or without persistent spiking did not differ significantly in their input resistance (153 ± 9 MΩ vs 162 ± 9 MΩ, mean ± SEM; $t_{170} = 0.76$, $p = 0.45$, *t* test) or resting membrane potential (−63 ± 1 mV vs −64 ± 1 mV; $t_{170} = -0.77$, $p = 0.44$, *t* test). We tested a variety of trigger stimuli but, to compare across neurons, all neurons were tested with trains of brief current pulses designed to evoke a reproducible number of spikes under different

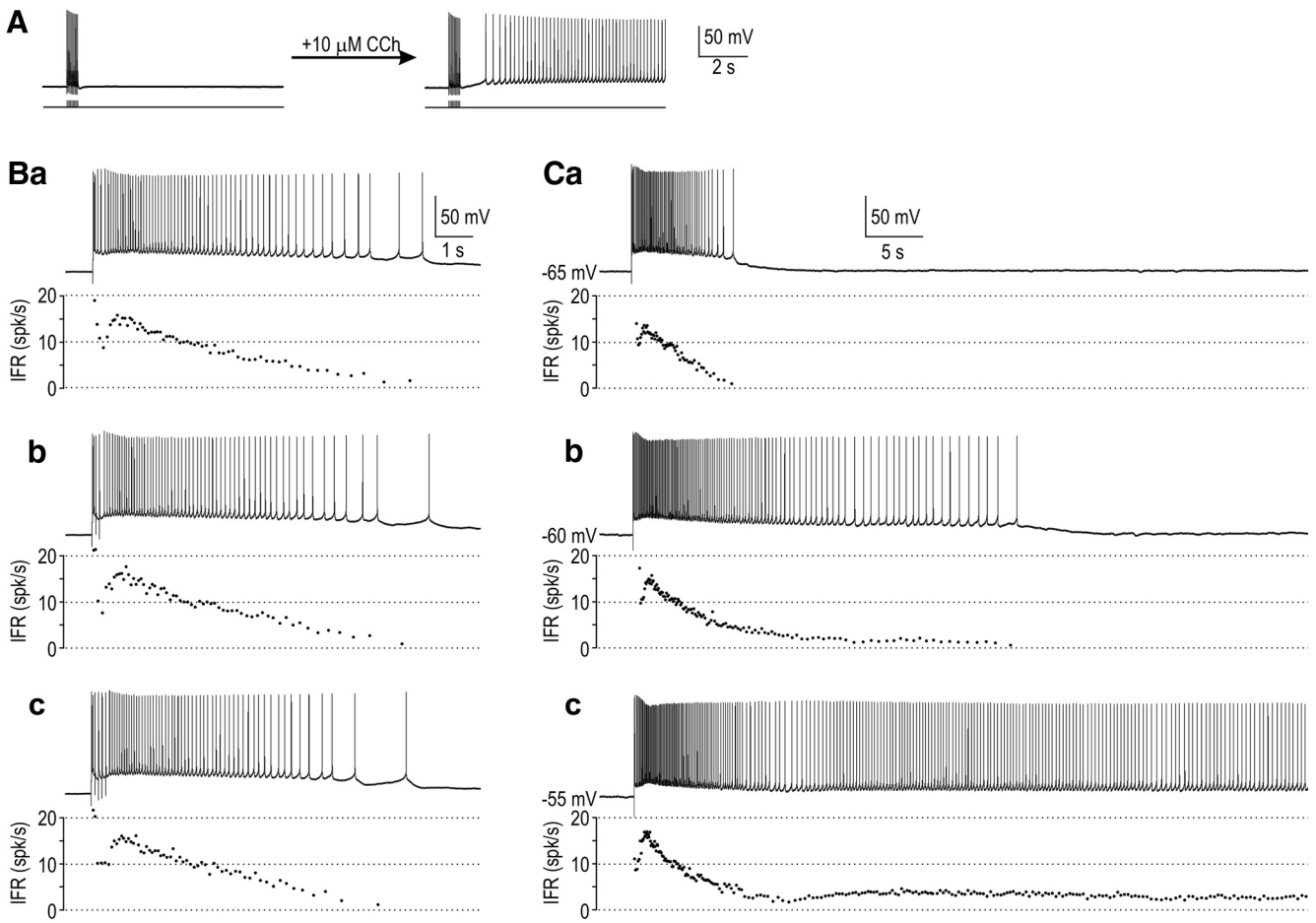

Figure 1. Persistent spiking in ACC pyramidal neurons. ***A***, Persistent spiking was observed only after muscarinic receptor activation. ***B***, Persistent spiking is insensitive to the number of spikes evoked by the trigger stimulus. From top to bottom (***Ba***–***Bc***), we applied 1, 3, or 5 current pulses respectively (4-ms-long, 200 pA). In this and subsequent panels, the IFR calculated from the reciprocal of the interspike interval and plotted at the midpoint of each interval is shown below each trace. ***C***, Persistent spiking is affected by the pretrigger membrane potential. From top to bottom (***Ca***–***Cc***), membrane potential was adjusted to −65, −60, or −55 mV respectively by DC current injection that was left unchanged for the duration of the response.

pharmacological conditions. The number of evoked spikes required to trigger persistent spiking varied between cells, but, once triggered, persistent spiking was independent of the trigger; for example, the neuron in Figure 1*B* responded with 64, 65, or 62 spikes when triggered with 1, 3, or 5 4-ms-long current pulses, respectively. The instantaneous firing rate (IFR = reciprocal of the interspike interval) exhibited a remarkably similar profile in each case. In contrast, persistent spiking was significantly affected by variations in the prestimulus membrane potential; for example, a neuron given the same one-pulse trigger spiked for only a few seconds when triggered at a hyperpolarized membrane potential but continued spiking for several minutes when triggered at a more depolarized membrane potential (Fig. 1*C*).

After a trigger, spiking typically accelerated and then decelerated before stabilizing at a rate that continued unchanged for several minutes (Fig. 2*Aa*). The longest duration of spiking that we observed (before applying hyperpolarizing current to terminate the response) was 18 min. If depolarizing current was injected during persistent spiking, firing rate increased during each stimulus, transiently decreased immediately afterward, and then promptly returned to its original baseline (Fig. 2*Ab*), which is unlike the graded persistent spiking observed in entorhinal cortex (Egorov et al., 2002; see also below). Conversely, persistent spiking was modulated sensitively by current injected through the recording pipette once spiking had started (Fig. 2*B*), consistent with an attractor associated with elevated excitability as opposed to one with a particular firing rate. Persistent spiking was often slow to begin after the initial trigger, resulting in a "pause" between evoked and persistent spikes, especially when the trigger stimulus was strong such as that observed by Zhang et al. (2010). Spiking was similarly delayed after subsequently applied triggers (Figs. 2*Ab*, 3*Aa*), consistent with an afterhyperpolarization induced by trigger-evoked spiking (see below). Last, when persistent spiking was terminated by injection of hyperpolarizing current, persistent spiking could resume when hyperpolarization was discontinued after as long as 1 min (Fig. 2*Bc*), although, in most neurons, persistent spiking was not resistant to distractors >10 s. Rebound spikes may retrigger persistent spiking in neurons in which persistent spiking requires only a weak trigger. No systematic differences in persistent spiking were noted between L2/3 and L5 neurons.

We did not observe any neurons with a rate of persistent spiking that depended on the number or intensity of triggers. Because the capacity for graded persistent spiking has been observed to "wash out" (Reboreda et al., 2007), it is notable that we did not observe graded spiking even immediately after breakthrough when patching with CCh already in the bath (to avoid waiting for CCh effects, during which washout could occur). Moreover, in four of four neurons recorded with perforated patch, persistent spiking was not graded, rather, the rate of persistent spiking was

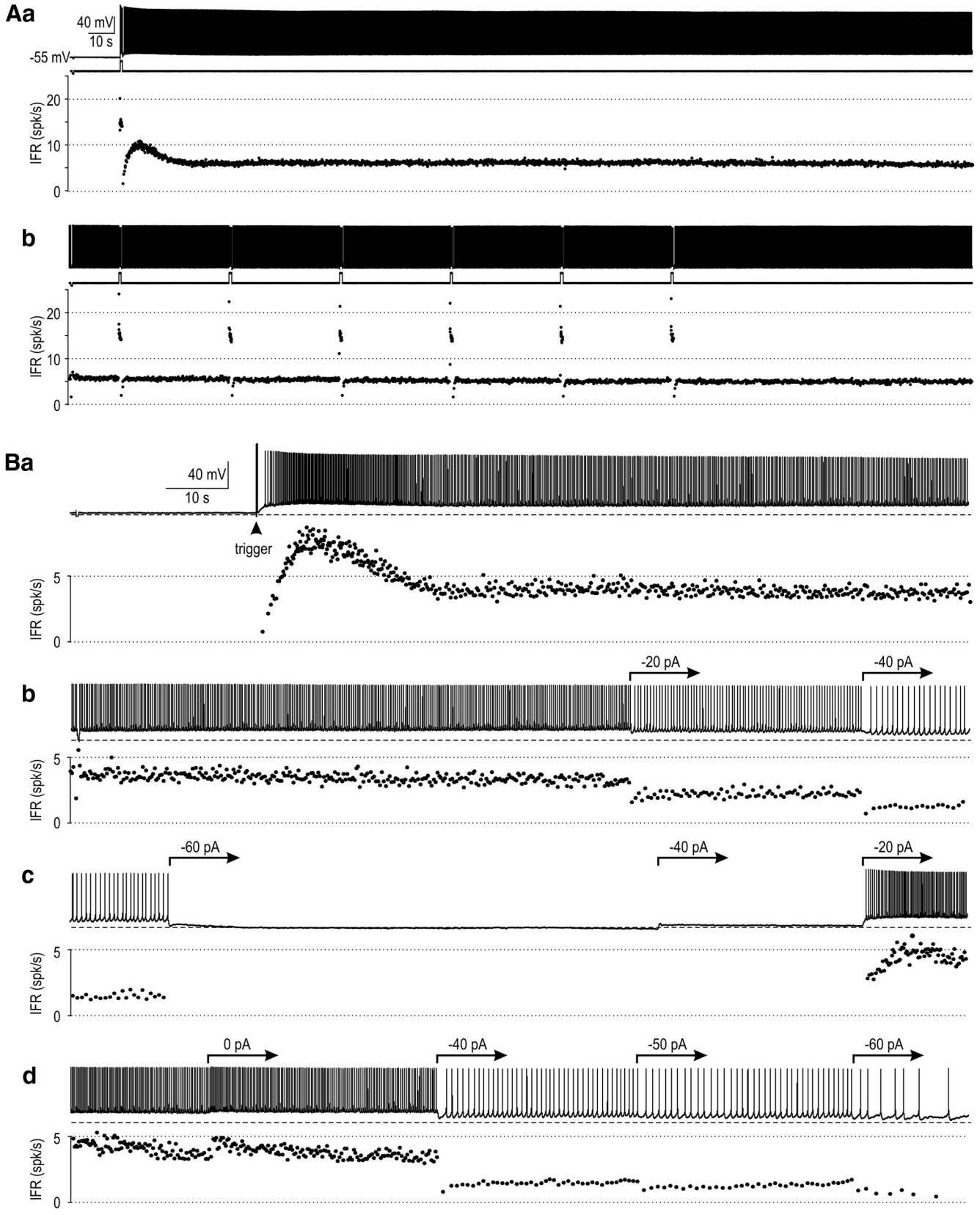

Figure 2. Stability and robustness of persistent spiking. ***A***, Once triggered, persistent spiking could continue at a remarkably stable rate for several minutes. Trace in ***Ab*** is continuation of the trace in ***Aa***. When depolarizing current was injected during persistent spiking, firing rate increased during stimulation, decreased transiently afterward, and then returned to the original rate. ***B***, Rate of persistent spiking could be increased or decreased by injection of modest current through the patch pipette. When persistent spiking was discontinued by injection of strong hyperpolarizing current, persistent spiking could resume upon release of that current without the need for stimulus-evoked spikes. Like at the onset of persistent spiking (***Ba***), IFR takes several seconds to stabilize at its steady-state value after the resumption of repetitive spiking following prolonged hyperpolarization (***Bc***) but changes quite quickly after small changes in current injection (***Bb***, ***Bd***). Resumption of persistent spiking after an imposed period of quiescence would support the robustness of working memory to distractors.

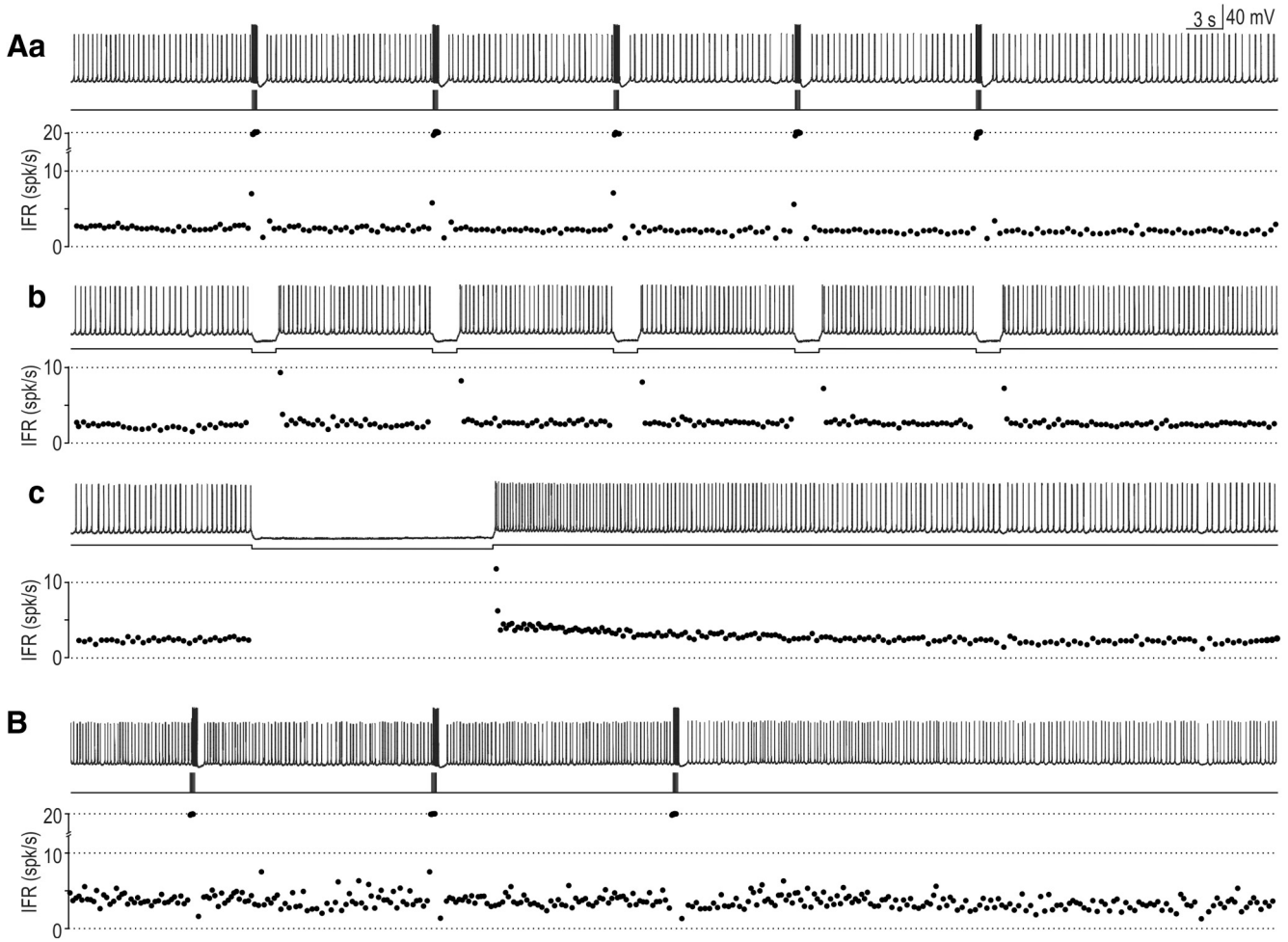

Figure 3. Persistant spiking characteristics are insensitive to recording method and temperature. ***A***, Sample perforated patch recording at room temperature. Trigger was applied before the start of trace in ***Aa***; traces in ***Ab*** and ***Ac*** are continuations of the same response. IFR returned to baseline after each train of 10 current pulses (***Aa***) and after each 25 pA hyperpolarizing step (***Ab***). Persistent spiking also resumed after a sustained (20-s-long) hyperpolarizing step (***Ac***). ***B***, Sample perforated patch recording at 31°C. Neurons recorded at 31°C in whole-cell mode exhibited the same pattern of persistent spiking illustrated here. There was no evidence of graded persistent spiking under any condition, including in response to longer trigger stimuli.

remarkably stable across repeated depolarizing pulse trains (Fig. 3*Aa*) and repeated hyperpolarizing steps (Fig. 3*Ab*). Persistent spiking was also able to resume after release from sustained hyperpolarization (Fig. 3*Ac*); in general, neurons recorded with perforated patch were resistant to longer distractors than neurons recorded with a ruptured patch. To test the effect of temperature, we slowly increased the bath temperature to 31°C and retested seven neurons that exhibited persistent spiking at room temperature. Five neurons continued to exhibit persistent spiking, whereas the other two exhibited plateau potentials that failed to reach spike threshold. The input resistance was 42 ± 4% less at 31°C than at room temperature ($t_4 = 2.89$, $p = 0.045$, paired t test), which is consistent with Lee et al. (2005) and may explain the reduced likelihood of I_{CAN} triggering persistent spiking, although we cannot rule out other temperature effects, for example, on VGCCs. That said, the persistent spiking observed at 31°C was never graded (Fig. 3*B*). In summary, neither the recording method nor the bath temperature affected the pattern of persistent spiking (cf. Figs. 3, 2). We cannot exclude that graded persistent spiking does not occur in ACC neurons under a condition we have not tested, but our data strongly suggest that the absence of graded persistent spiking in ACC neurons is a feature of those neurons rather than a reflection of experimental conditions.

Biophysical mechanism of persistent spiking in ACC pyramidal neurons

Next, we explored the role of TRPC channels in persistent spiking and the associated changes in intracellular calcium. First, we verified that persistent spiking was blocked by application of 100 μM flufenamic acid, an antagonist of I_{CAN} ($n = 6$ cells; Fig. 4*A*), or by application of 50–100 μM SKF-96365, a selective antagonist of TRPC channels ($n = 10$ cells; Fig. 4*B*). To verify the necessity of elevated intracellular calcium for TRPC channel activation, we compared responses in the same neuron before and after photoactivating an intracellularly loaded, caged calcium chelator diazo-2. In four of four neurons tested, activation of diazo-2 by UV light during persistent spiking caused persistent spiking to stop and prevented it from being retriggered by subsequent stimuli, although evoked spikes were unchanged (Fig. 4*C*). Not even an afterdepolarization was evident after diazo-2 activation, consistent with calcium buffering preventing I_{CAN} activation. Application of equivalent UV light to neurons not loaded with diazo-2 did not affect persistent spiking. Application of 2 μM thapsigargin to disrupt calcium-induced calcium release from intracellular stores did not have any effect on persistent spiking ($n = 3$ cells; Fig. 4*D*).

When a trigger stimulus was applied but persistent spiking was prevented by promptly hyperpolarizing the neuron after

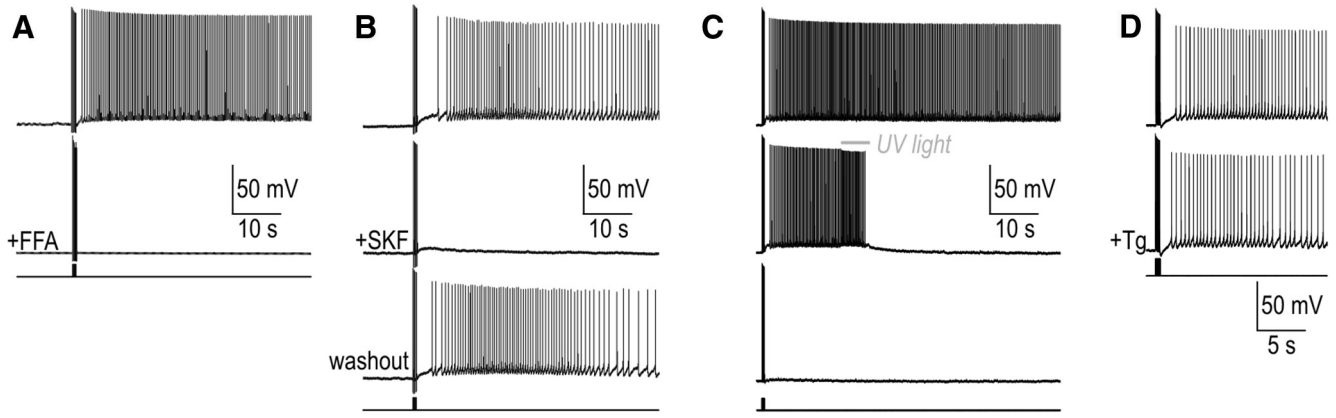

Figure 4. Involvement of TRPC channels and the necessity of intracellular calcium signaling. All experiments were performed in the presence of CCh. ***A***, Persistent spiking was blocked in 6 of 6 neurons tested by 100 μM flufenamic acid (FFA), an antagonist of I_{CAN}. ***B***, Persistent spiking was also blocked in 10 of 10 neurons by 50–100 μM SKF-96365, which is a more selective TRPC antagonist. ***C***, In four of four neurons tested, photoactivation of the calcium buffer diazo-2 caused persistent spiking to be terminated (middle trace) and prevented from being retriggered (bottom trace). For these experiments, 2 mM diazo-2 was included in the pipette solution. The change in spike amplitude during UV irradiation is likely due to a photoelectric effect; spikes evoked after irradiation were unchanged from those evoked before irradiation. ***D***, Persistent spiking was not blocked in three of three neurons in which calcium-induced calcium release was disrupted by 2 μM thapsigargin (Tg).

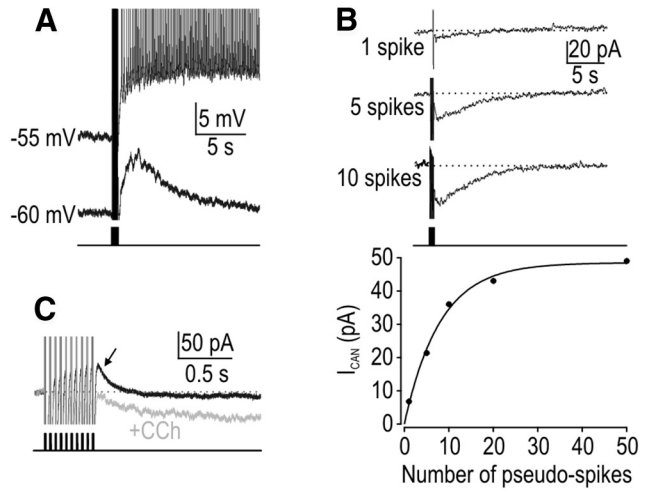

Figure 5. Spike-evoked currents. ***A***, Example of persistent spiking (top) and afterdepolarization (bottom) evoked by the same trigger but with the cell adjusted to different membrane potentials. Whereas persistent spiking continued until eventually terminated by hyperpolarizing current injection, afterdepolarizations (plateau potentials) lasted only a few seconds. ***B***, In voltage-clamp experiments (in the presence of 1 μM TTX to prevent unclamped spikes), holding potential was stepped from −50 mV to +50 mV for 5 ms to approximate VGCC activation that occurs during a spike. Graph shows peak inward current after different numbers of pseudospikes based on cell for which sample responses are shown above. Exponential curve fits from three neurons tested revealed half-maximal activation at 4.9 ± 0.3 pseudospikes. Based on systematic testing with 10 pseudospikes, peak inward current was 43 ± 5 pA and the deactivation time constant was 5.8 ± 0.7 s (mean ± SEM; $n = 9$ neurons). ***C***, Equivalent voltage-clamp protocol applied before CCh (black trace) revealed an outward current (arrow). Based on testing with 10 pseudospikes, peak outward current was 53 ± 10 pA and the deactivation time constant was 305 ± 59 ms ($n = 6$ neurons). The outward current is obscured by the inward current that develops after CCh (gray trace). Although the magnitudes of the two spike-evoked currents are similar, the inward current persists much longer than the outward current; the net current dictates the latency to persistent spiking.

stimulation, we observed an afterdepolarization that decayed on a time scale of seconds (Fig. 5*A*). A deactivation time constant of 5.8 ± 0.7 s ($n = 9$ neurons) was observed in voltage-clamp recordings when holding potential was stepped to +50 mV for 5 ms intervals to approximate trigger spikes before clamping the membrane potential back at −50 mV to measure the resulting current (Fig. 5*B*). The peak inward current evoked by 10 pseudospikes delivered at 20 Hz was 43 ± 5 pA. The graph in Figure 5*B* shows that the inward current saturates as the number of pseudospikes is increased, with half-maximal activation achieved at 4.9 ± 0.3 pseudospikes under the conditions tested ($n = 3$ neurons); this saturation is consistent with previous experiments (Sidiropoulou et al., 2009) and simulations (Fransen et al., 2002). The same voltage-clamp protocol applied before CCh revealed an outward current with amplitude of 53 ± 10 pA and decay time of 305 ± 59 ms ($n = 6$ neurons) (Fig. 5*C*, black trace); this outward current is obscured by the inward current that develops after CCh (Fig. 5*C*, gray trace). These results suggest that, in the presence of CCh, spikes evoke inward (depolarizing) and outward (hyperpolarizing) currents of approximately equal amplitude, but the former persists an order of magnitude longer than the latter. The time taken for the outward current to wane accounts for the pause between evoked and persistent spiking (see also simulations below). One should also notice that, although the decay rate of inward current and the resulting afterdepolarization is quite slow, it is still fast compared with persistent spiking, which can persist for minutes (cf. Fig. 5*A*, top trace). We hypothesized that persistent spiking maintains elevated intracellular calcium and thereby sustains I_{CAN} activation, but that in the absence of continued spiking, I_{CAN} will deactivate at a rate proportional to how fast calcium is cleared from the cytosol, which occurs with a time constant of seconds (see below). This raises important questions about how intracellular calcium concentration ($[Ca^{2+}]_i$) changes during the early (activation) and late (maintenance) phases of persistent spiking.

Previous studies found that nifedipine, an antagonist of L-type calcium channels, blocks CCh-induced persistent spiking (see Introduction). Because L-type calcium channels are activated at voltages that normally occur only during spikes, the nifedipine effect suggests that spikes are necessary for the calcium that activates I_{CAN}. That said, spike-dependent calcium influx may be necessary for the initial activation of I_{CAN}, but calcium influx via I_{CAN} itself could conceivably maintain I_{CAN} activation. To investigate the role of spikes in maintaining I_{CAN} activation, we combined current-clamp recordings with calcium imaging using intracellularly loaded Calcium Green-1 (see Materials and Methods). Imaging revealed that intracellular calcium increased during evoked spiking and remained elevated during persistent spiking, but returned to baseline in the absence of spiking (Fig. 6*A*). Calcium returned to baseline with the same kinetics in the

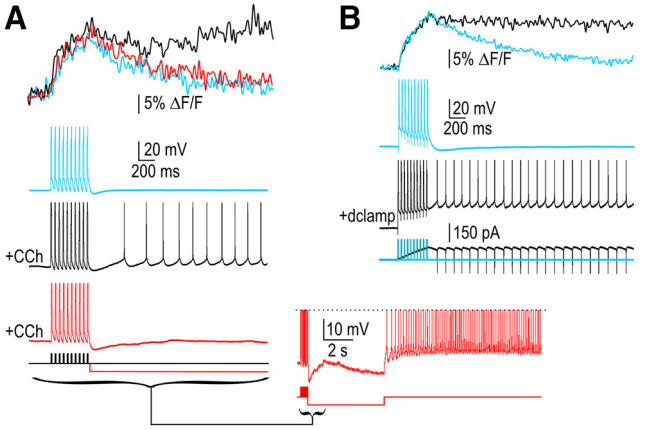

Figure 6. Necessity and sufficiency of spikes for $[Ca^{2+}]_i$ changes associated with persistent spiking. Data in this figure are based on wide-field fluorescence imaging of Calcium Green-1. ***A***, Calcium responses were monitored before CCh (blue), after CCh (black), and after CCh, but with persistent spiking prevented by poststimulus hyperpolarization (red). Trigger stimuli caused an equivalent increase in calcium in each condition, but whereas calcium returned to baseline within few hundred milliseconds in the absence of persistent spiking, it remained elevated when spiking continued, thus arguing that spikes are necessary for the calcium dynamics associated with persistent spiking. Bottom trace shows compressed view of red trace to highlight the afterdepolarization revealed when persistent spiking is blocked. This sample response also shows that persistent spiking developed when hyperpolarizing current was released, reminiscent of the resumption of repetitive spiking illustrated in Figure 2*B*. ***B***, Dynamic clamp was used to insert a virtual CAN-like current (see Materials and Methods). The electrophysiological response demonstrates sufficiency of CAN current to cause persistent spiking. However, whereas native CAN current may involve calcium flux that could contribute to the calcium signal, the virtual CAN current does not; therefore, it is notable that the calcium signal during persistent spiking mediated by virtual CAN current (black) was the same as that mediated by native CAN current (cf. black trace in ***A***), which argues that spike-mediated calcium entry is sufficient to explain the calcium signal associated with persistent spiking.

absence of I_{CAN} activation (i.e., without CCh) and when I_{CAN} was activated but persistent spiking was prevented by immediate poststimulus hyperpolarization (cf.Fig. 6*A*, blue and red traces). This pattern, which was observed from within-cell comparisons in three of three neurons tested, argues that spiking is necessary to sustain the elevated calcium required for persistent spiking.

To test the sufficiency of persistent spiking to maintain elevated calcium levels, we turned to dynamic clamp. Rather than applying CCh to enable activation of native I_{CAN}, we used dynamic clamp to introduce virtual I_{CAN}. Importantly, virtual I_{CAN} is mediated by current injected through the patch pipette and does not therefore involve calcium influx, but the resulting spikes nonetheless activate native L-type calcium channels. In four of four neurons tested, the introduction of virtual I_{CAN} caused persistent spiking and a sustained increase in $[Ca^{2+}]_i$ (Fig. 6*B*), thus arguing that calcium entry during spikes is sufficient to account for the calcium dynamics seen during persistent spiking mediated by native I_{CAN} (cf. Fig. 6*A*). The dynamic-clamp data also demonstrate the sufficiency of a CAN-like current to mediate persistent spiking. Because $[Ca^{2+}]_i$ cannot be measured at the rate (20 kHz) required for real-time feedback to our dynamic-clamp model, the virtual CAN current was modeled as a voltage-dependent current that activates only during suprathreshold voltage deflections (see Materials and Methods).

To measure calcium clearance kinetics, additional imaging experiments were conducted using two-photon microscopy (see Materials and Methods). For these experiments, an increase in $[Ca^{2+}]_i$ was caused by spiking entrained at a specified rate by a stimulus train (Fig. 7*A*) or by persistent spiking (Fig. 7*B*). The decay in fluorescence when the stimulus train ended or persistent

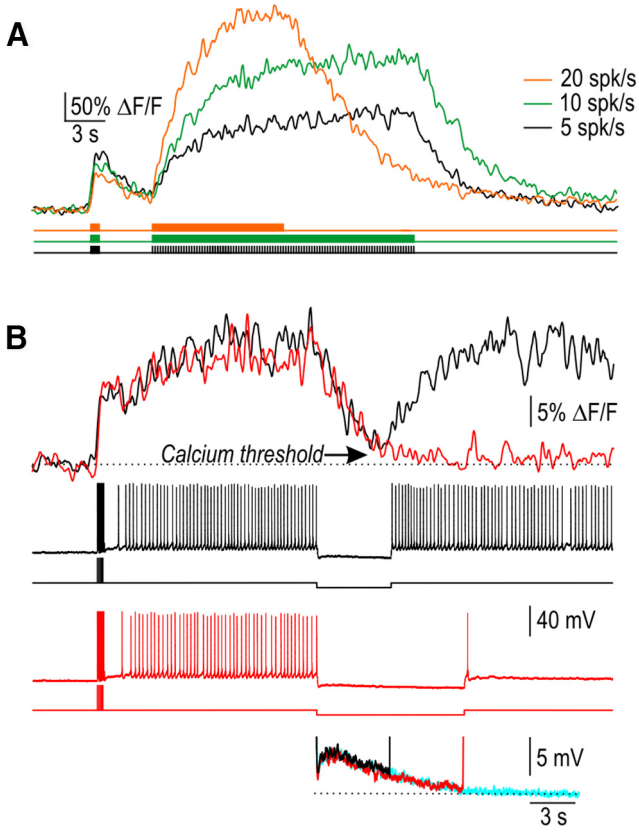

Figure 7. Characterization of $[Ca^{2+}]_i$ kinetics and their association with persistent spiking. Data in this figure are based on two-photon imaging of Fluo-4. ***A***, Sample calcium responses from a typical neuron to a trigger (10 depolarizing pulses over 500 ms) followed by spiking entrained by depolarizing pulses delivered at 5, 10, or 20 Hz. Return of fluorescence intensity to baseline at the end of stimulation was well fit by a monoexponential process with $\tau_{Ca} = 3.3$, 4.0, or 5.6 s for stimulation at 5, 10, or 20 Hz, respectively. These data also show that $[Ca^{2+}]_i$ increases with firing rate and that the dye is not saturated at low firing rates. ***B***, Sample calcium responses during persistent spiking. When persistent spiking was terminated by injection of hyperpolarizing current, fluorescence intensity decayed with $\tau_{Ca} = 2.4$ s. Persistent spiking resumed when hyperpolarization was terminated after 5 s, before $[Ca^{2+}]_i$ returned to baseline (black traces). Persistent spiking did not resume after longer hyperpolarization, consistent with $[Ca^{2+}]_i$ having returned to baseline (red traces). Traces at bottom show vertically enlarged view of voltage traces to compare plateau potential; blue trace shows response during 20-s-long hyperpolarizing step to confirm that voltage returned to baseline by ~10 s.

spiking was terminated by injection of hyperpolarizing current was well fit by a monoexponential process; we never observed any late increases in $[Ca^{2+}]_i$ comparable to what El-Hassar et al. (2011) reported. The decay τ of 4.6 ± 1.6 s for the calcium-dependent fluorescence signal ($n = 4$ neurons) is similar to previously reported values (Abel et al., 2004) and did not differ significantly from the I_{CAN} deactivation τ of 5.9 ± 0.7 s ($t_{11} = 0.78$, $p = 0.46$, t test). This suggests that the rate of deactivation of I_{CAN} is governed by the changes in $[Ca^{2+}]_i$, but we cannot exclude that other processes sustain I_{CAN} activation longer than $[Ca^{2+}]_i$ is elevated. Indeed, this may be necessary to explain the resumption of persistent spiking after very long distractors (>20 s), but resistance to such long distractors is exceptional. Responses illustrated in Figure 7*B* are more typical. Persistent spiking resumed at the end of a 5-s-long hyperpolarizing step (Fig. 7*B*, black traces), consistent with $[Ca^{2+}]_i$ (Fig. 7*B*, top) and the plateau potential (Fig. 7*B*, bottom) having not yet returned to baseline, which means that the calcium threshold lies somewhere below the inflection point on the top trace. In comparison, at the end of a 10-s-long hyperpolarizing step (Fig. 7*B*, red traces), per-

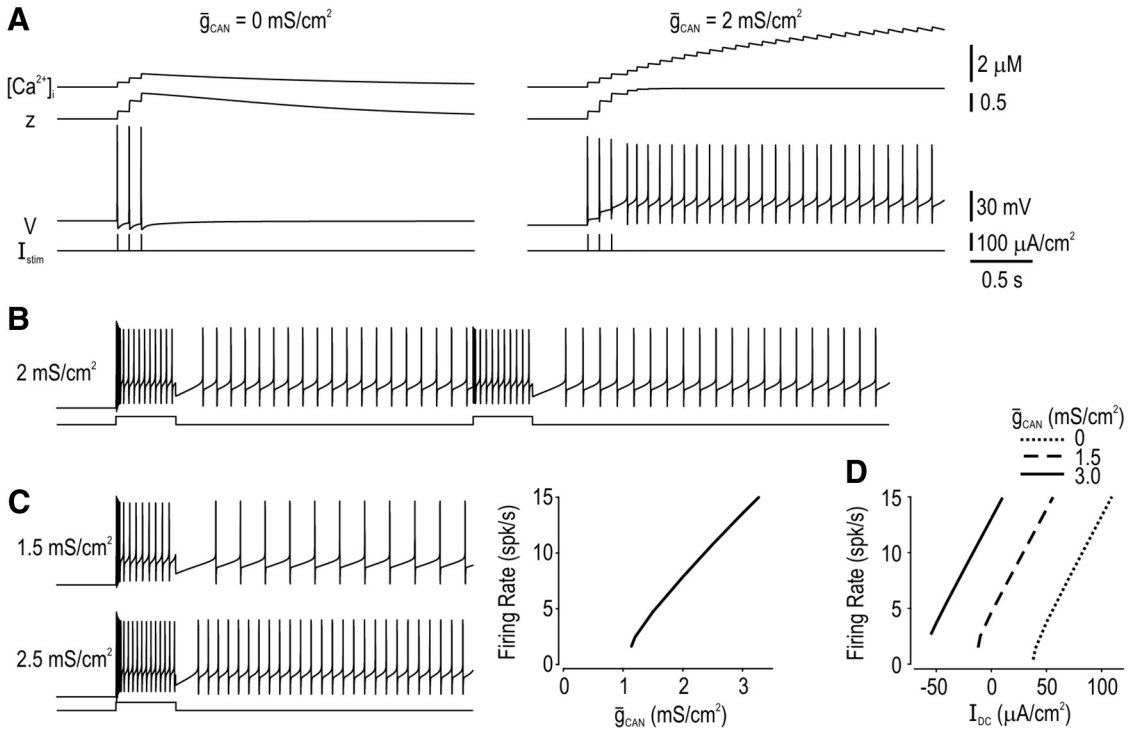

Figure 8. Persistent spiking in a neuron model. ***A***, Responses of a neuron model without (left) and with (right) $\bar{g}_{CAN} = 2$ mS/cm^2. Three short current pulses triggered persistent spiking only in the latter case. ***V***, Voltage; $[Ca^{2+}]_i$, intracellular calcium concentration; *z*, gating variable for g_{CAN}. Scale bars apply to all subsequent panels. ***B***, Rate of persistent spiking is unaffected by the number of triggers (cf. spiking before and after second current step) and by the trigger intensity (cf. spiking here with spiking in ***A***). The rate of persistent spiking varies with $\bar{g}_{CAN}$ (***C***) and with DC current (***D***). Curves in ***D*** show that $\bar{g}_{CAN}$ controls the offset, but not the gain, of the input–output curve.

sistent spiking did not resume, consistent with $[Ca^{2+}]_i$ and the plateau potential having returned to baseline. The blue trace in Figure 7*B* shows the plateau during an even longer hyperpolarizing step to confirm baseline. These data also indicate persistent spiking can drive $[Ca^{2+}]_i$ much higher than the minimum (threshold) level required for persistent spiking. Overall, these data are consistent with spike-mediated calcium influx causing large increases in $[Ca^{2+}]_i$ that saturate the activation of I_{CAN}.

Dynamical mechanism of persistent spiking in a computational model

The experimental data reported above establish that evoked spiking is necessary and sufficient to cause the calcium influx that (contingent on muscarinic receptor activation) triggers an inward CAN current mediated by TRPC channels. The CAN current is sufficient to drive spiking, thus maintaining the elevated intracellular calcium required to sustain I_{CAN} activation. This explanation identifies spike-mediated calcium influx as a key intermediary in the positive feedback loop between spiking and TRPC activation, but this in itself does not explain many features of the persistent spiking that we observed, such as how persistent spiking can resume after a prolonged period of hyperpolarization-imposed quiescence. To facilitate deeper analysis into how biophysical mechanisms may interact to produce the pattern of persistent spiking exhibited by ACC neurons (and whether known mechanisms, acting together, are indeed sufficient to explain persistent spiking), we built a computational model constrained by the biophysical details described above and previously reported in the literature (see Materials and Methods).

Using a one-compartment model with spiking controlled by Morris–Lecar equations, we added high-threshold VGCCs, a first-order calcium clearance mechanism, and a calcium-activated, nonspecific cation current (I_{CAN}). We also included afterhyperpolarization currents (I_{AHP}) to account for spike rate adaptation and the outward current observed in voltage-clamp experiments (Fig. 5*C*). Figure 8*A* illustrates the persistent spiking enabled by inclusion of I_{CAN}. Under the conditions simulated, persistent spiking was triggered by as few as three evoked spikes. The minimum number of trigger spikes depends jointly on calcium channel density, $\bar{g}_{Ca}$, and TRPC channel density, $\bar{g}_{CAN}$; the former controls the amount of calcium influx (per spike) and the latter controls how much total I_{CAN} is activated by a given increase in $[Ca^{2+}]_i$. According to these simulations, g_{CAN} becomes maximally activated after only a few spikes, as evident by saturation of its gating variable *z* (consistent with Fig. 5*B*), whereas $[Ca^{2+}]_i$ continues to increase to a steady-state value that depends on firing rate. Though we have emphasized cholinergic modulation of $\bar{g}_{CAN}$, voltage-gated calcium currents (i.e., $\bar{g}_{Ca}$) could also be modulated.

As in experiments (Figs. 1*B*, 2*A*, 3*A*,*B*), the rate of persistent spiking in our computational model did not depend on the intensity or number of triggers (cf. responses in Fig. 8*A*,*B*). Instead, the model demonstrates that because I_{CAN} is maximally activated, its magnitude is dictated by $\bar{g}_{CAN}$ (Fig. 8*C*), which is regulated on a slower timescale by muscarinic receptor activation (see Discussion). This saturation explains why I_{CAN} is activated in a switch-like manner rather than being proportional to firing rate, and that decoupling in turn explains the lack of runaway positive feedback between persistent spiking and I_{CAN} activation, and why the rate of persistent spiking is not regulated by graded I_{CAN} activation. Instead, the rate of persistent spiking can be modulated by current injection (Fig. 8*D*), consistent with experimental data shown in Figure 2. Plotting firing rate as a function of DC current for neuron models with different $\bar{g}_{CAN}$ reveals that different TRPC

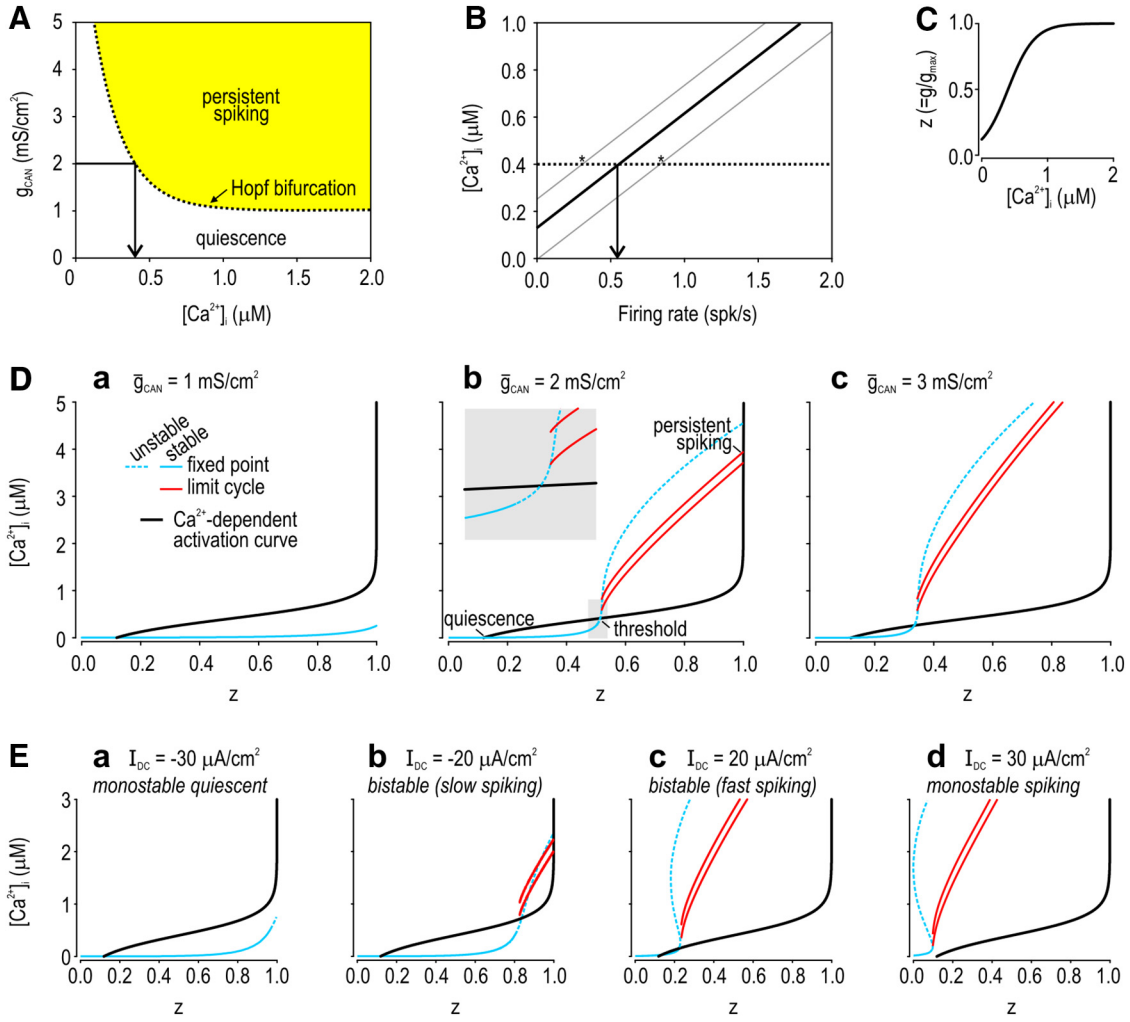

Figure 9. Dynamical analysis of persistent spiking. ***A***, 2D bifurcation analysis shows the combinations of $[Ca^{2+}]_i$ and $\bar{g}_{CAN}$ at which the system undergoes a Hopf bifurcation (dotted line). For this analysis, $[Ca^{2+}]_i$ was converted from a dynamic variable to a parameter the value of which was varied systematically. ***B***, To find the firing rate at which $[Ca^{2+}]_i$ reaches threshold, we plotted the maximum and minimum $[Ca^{2+}]_i$ within each interspike interval for different firing rates (gray lines). Dotted line shows threshold $[Ca^{2+}]_i$ identified in ***A*** for $\bar{g}_{CAN} = 2$ mS/cm^2. The rate of evoked spiking required to trigger persistent spiking must lie somewhere between the two intersection points marked with an asterisk. The minimum rate of trigger spikes was empirically determined to be 0.54 spikes/s, from which we extrapolate the "effective" $[Ca^{2+}]_i$ as a function of firing rate (solid black line). ***C***, Plot showing calcium sensitivity of *z*, the gating variable for g_{CAN}. ***D***, 1D bifurcation analysis shows how high *z* must increase to trigger persistent spiking. Analysis was repeated in models with three different values of $\bar{g}_{CAN}$ (***Da–Dc***). Bifurcation plot includes a stable fixed point (solid blue curve) representing quiescence and a stable limit cycle (solid red curves) representing regular repetitive spiking. Black plot represents the activation curve shown in ***C***. The activation curve intersects the bifurcation diagram at three locations (labeled on ***Db***) that predict how the full system (i.e., with *z* treated as a dynamic variable) will evolve. Evoked spiking causes *z* to increase, but, when stimulation ends, *z* will diverge from the threshold toward either the left or right intersection, which corresponds to quiescence and persistent spiking, respectively. ***E***, 1D bifurcation analysis was repeated for a model with $\bar{g}_{CAN} = 2$ mS/cm^2, but with different DC current injection (***Ea–Ed***); the key observation is how the bifurcation diagram (blue and red curves) intersect the TRPC activation curve (black). Strong hyperpolarizing current precludes persistent spiking by increasing the threshold value of *z* so high that no bifurcation occurs (***Ea***), whereas strong depolarizing current leads to spontaneous spiking by reducing the threshold value of *z* to a level that can be achieved without any evoked spiking (***Ed***); in both cases, the curves do not intersect in a way conducive to bistability. Intermediate stimuli (***Eb***, ***Ec***) shift the threshold (middle intersection point) and $[Ca^{2+}]_i$ at steady-state (rightmost intersection point) but, in either case, I_{CAN} becomes maximally activated (*z* converges on 1) if threshold is reached.

channel densities shift the input–output curve without affecting gain (Fig. 8*D*). In other words, the active state is associated with a bias current of fixed amplitude provided by the switch-like activation of available TRPC channels. Our model also reproduced the resumption of persistent spiking after a period of hyperpolarization-imposed quiescence, but an explanation of this phenomenon is deferred until after the bifurcation analysis described below.

Having reproduced the key features of persistent spiking in our model, we next sought to study the nonlinear dynamics exhibited by the model. To start, we conducted 2D bifurcation analysis using $[Ca^{2+}]_i$ and $\bar{g}_{CAN}$ as bifurcation parameters. Specifically, rather than treating $[Ca^{2+}]_i$ as an internally controlled variable, we converted it to a parameter to determine the level of $[Ca^{2+}]_i$ as a function of $\bar{g}_{CAN}$, at which the neuron begins spiking repetitively (Fig. 9*A*). For example, for $\bar{g}_{CAN} = 2$ mS/cm^2, the system underwent a Hopf bifurcation when $[Ca^{2+}]_i$ reached 0.40 μM, implying that TRPC channels were sufficiently activated to support persistent spiking. For lower $\bar{g}_{CAN}$, a greater increase in $[Ca^{2+}]_i$ was required, but no increase was sufficient to cause persistent spiking for $\bar{g}_{CAN}$ as low as 1 mS/cm^2. To verify the accuracy of this bifurcation analysis, we plotted the threshold $[Ca^{2+}]_i$ level (dotted line) together with maximum and minimum $[Ca^{2+}]_i$ achieved during different steady-state firing rates (solid gray lines) for a model with $\bar{g}_{CAN} = 2$ mS/cm^2 (Fig. 9*B*). Consistent with experimental data (Helmchen et al., 1996; Abel et

al., 2004), $[Ca^{2+}]_i$ increased linearly with firing rate (see also Fig. 7*A*). The intersection of the gray lines with the dotted line predicts that the minimum firing rate required to trigger persistent spiking is between 0.31 and 0.82 spikes/s. Based on simulations in the original model (i.e., with $[Ca^{2+}]_i$ treated as a variable), the minimum rate was determined empirically to be 0.54 spikes/s. From this, we extrapolated the relationship between firing rate and effective $[Ca^{2+}]_i$ (Fig. 9*B*, solid black line). To illustrate how strongly g_{CAN} is activated by these calcium changes, Figure 9*C* shows z, the gating variable for g_{CAN} as a function of $[Ca^{2+}]_i$. This activation curve is projected onto the bifurcation diagrams in Figure 9, *D* and *E*, with the x- and y-axes flipped relative to the presentation in Figure 9*C*. Exact values depend on the value of other parameters such as τ_{Ca}, but the dynamics are qualitatively unchanged over a broad range of plausible values (data not shown).

In Figure 9*D*, we systematically varied z in models with different $\bar{g}_{CAN}$. For $\bar{g}_{CAN} = 1$ mS/cm^2, maximal activation of TRPC channels was insufficient to cause a bifurcation (Fig. 9*Da*), consistent with data in Figure 8*A*. For $\bar{g}_{CAN} = 2$ mS/cm^2, the fixed point destabilized at $z = 0.503$, which marks the onset of spiking, although a stable limit cycle (representing regular repetitive spiking) did not appear until $z = 0.519$ (Fig. 9*Db*); for intervening values of z, repetitive spiking occurred but with irregular interspike intervals. A similar pattern was observed for $\bar{g}_{CAN} = 3$ mS/cm^2, but bifurcations occurred at smaller values of z (Fig. 9*Dc*). Destabilization of the fixed point and emergence of a stable limit cycle occurred near where the blue curve representing the fixed point crossed the black curve representing I_{CAN} activation, suggesting that that intersection represents the I_{CAN} activation threshold that must be reached for persistent spiking to ensue. When z is treated as a variable, positive feedback activation of I_{CAN} will drive continued spiking when/if evoked spiking causes calcium to increase high enough that z reaches this threshold. This analysis further predicts that once persistent spiking starts, the system will diverge from threshold to stabilize at the intersection of the red limit cycle curves with the black activation curve, which implies that I_{CAN} becomes maximally activated. If evoked spiking does not increase calcium enough to reach threshold, then the system will return to the intersection of the fixed-point curve with the black activation curve. The bottom left and top right intersections thus represent two attractors, one representing quiescence and the other representing persistent spiking, that are separated by a threshold (see labeling on Fig. 9*Db*).

We repeated bifurcation analysis in the model with $\bar{g}_{CAN} = 2$ mS/cm^2 with different levels of DC current injection (Fig. 9*E*). Injection of sufficiently strong hyperpolarizing current prevented any bifurcation from occurring as z was increased (Fig. 9*Ea*). Modest hyperpolarizing current delayed the bifurcation and reduced the $[Ca^{2+}]_i$ at steady state (Fig. 9*Eb*), consistent with the reduced firing rate at steady state. Modest depolarizing current had the opposite effect (Fig. 9*Ec*) and strong depolarizing current caused spontaneous spiking, which is to say that the blue fixed point curve no longer intersected the black activation curve, implying a single attractor state corresponding to repetitive spiking (Fig. 9*Ed*).

The analysis above explains that $[Ca^{2+}]_i$ can stabilize at different values during persistent spiking. If persistent spiking is stopped (e.g., by hyperpolarizing current injection), then $[Ca^{2+}]_i$ must drop significantly before crossing back over its threshold to a state of quiescence; furthermore, given the nonlinear relationship between $[Ca^{2+}]_i$ and I_{CAN} activation (Fig. 8*C*), I_{CAN} remains fully activated until $[Ca^{2+}]_i$ decreases below ~1 μM. If hyperpolarization is discontinued before z crosses back across its threshold, then persistent spiking can resume (Fig. 10*A*). If persistent spiking is interrupted sooner after its initiation, before $[Ca^{2+}]_i$ reaches steady state, then the maximum duration of quiescence after which persistent spiking can resume is predictably shorter (Fig. 10*B*). An increase in calcium higher than required to activate TRPC channel maximally can thus explain the robustness of persistent spiking to distractors yet is consistent with the monoexponential calcium decay observed experimentally (Fig. 7). Our computational model was resistant to distractors up to 5 s long (= 2.5× longer than τ_{Ca} of 2 s). Extrapolating from our experimentally measured τ_{Ca} of 3.4 s, we predict resistance to distractors up to 8.5 s long (and up to 21 s based on the upper range of τ_{Ca}); most neurons fall within the lower range. Resistance to longer distractors (Figs. 2*Bc*, 3*Ac*) suggests that calcium clearance in certain neurons or from certain compartments (e.g., microdomains) may be slower than suggested by our calcium imaging data or that gating of I_{CAN} lags behind changes in $[Ca^{2+}]_i$. Rebound spikes may also retrigger persistent spiking. The observation that neurons recorded with perforated patch could resume spiking after particularly long distractors is arguably because calcium clearance is slower under those conditions because, unlike in whole-cell (ruptured patch) recordings, cytosolic calcium does not equilibrate with the calcium-free pipette solution. Imaging experiments using calcium sensors not loaded via a patch pipette are required to test this, which is obviously important, along with network mechanisms, for understanding persistent spiking under realistic *in vivo* conditions.

Discussion

In this study, we demonstrated how robust persistent spiking can arise from the nonlinear relationship between intracellular calcium and TRPC channel activation. We found that as few as one evoked spike can cause calcium influx sufficient to activate enough I_{CAN} to drive another spike, thus establishing a positive feedback loop in which spiking maintains activation of I_{CAN} and vice versa. Indeed, spikes are necessary and sufficient for the calcium influx required for TRPC channel activation. Our results further suggest that I_{CAN} activation saturates after calcium levels exceed the threshold for persistent spiking, thus preventing runaway positive feedback by decoupling the degree of I_{CAN} activation from the absolute level of calcium. Therefore, I_{CAN} is turned on and off in a switch-like manner (Figs. 9, 10). The availability of functional TRPC channels, based on their translocation to the cell surface (Tai et al., 2011), is controlled separately by metabotropic receptor signaling via phospholipase C (PLC) (Mori et al., 2015). Many aspects of this joint control by calcium and PLC remain to be explored, but simulations provide valuable insights. In any case, because available TRPC channels activate in an all-or-none manner, they provide a fixed amount of depolarizing current. This current shifts the neuron to a more excitable state, so much so that spiking can continue without external input (although the neuron remains responsive to input; see below). Because I_{CAN} activation is switch like, persistent spiking is not maintained at a fixed rate; instead, external inputs can add to or subtract from the bias current mediated by I_{CAN}, thus enabling the neuron to modulate its firing rate to encode ongoing, previously subthreshold input contingent on (i.e., with memory of) a preceding suprathreshold trigger. Variation in the rate of persistent spiking is consistent with *in vivo* data (Brody et al., 2003) and will also affect how an intrinsically bistable neuron operates within a recurrently connected network (Fransen et al., 2002; Jochems and Yoshida, 2015; Giovannini et al., 2017). The robust-

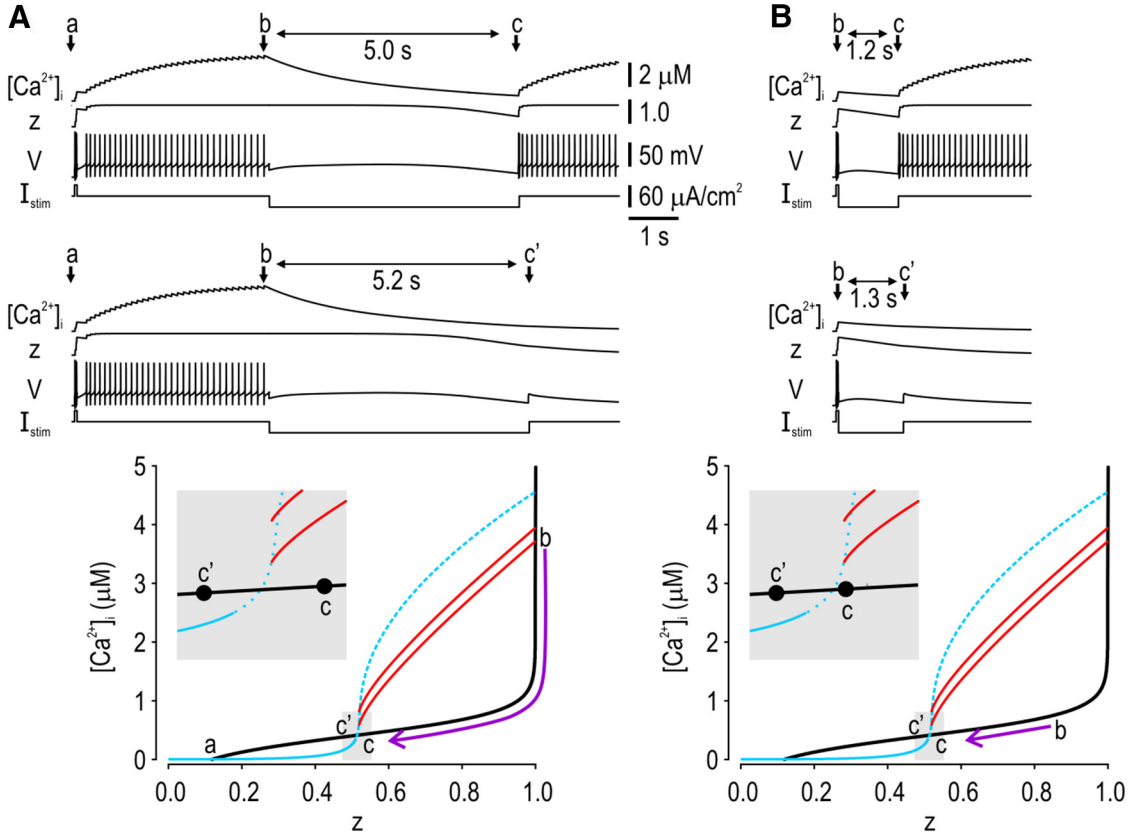

Figure 10. Resumption of persistent spiking and its dynamical basis. Simulations are based on a neuron model with $\bar{g}_{CAN} = 2$ mS/cm^2. ***A***, Hyperpolarizing step sufficient to stop spiking caused $[Ca^{2+}]_i$ to fall but *z* remained high until $[Ca^{2+}]_i$ dropped below ~1 μM. Time points ***a***–***c*** on the sample traces are marked on the bifurcation diagram. The resumption of persistent spiking upon release from hyperpolarization was predicted by whether *z* dropped below threshold (cf. ***c*** and ***c'***). ***B***, If hyperpolarization is applied early after the trigger, before intracellular calcium has reached the steady-state level associated with persistent spiking (cf. the lengths of the purple arrow in ***B*** with that in ***A***), then persistent spiking is more readily disrupted.

ness of persistent spiking to distractors also emerges from the decoupling of I_{CAN} activation from calcium level. By calcium rising higher than needed to activate TRPC channels fully, calcium can drop significantly from its peak levels before I_{CAN} starts to deactivate, which means persistent spiking can resume after prolonged periods of quiescence. We conclude that TRPC channels are sufficient to mediate persistent spiking in ACC neurons, but the details of that spiking emerge from the nonlinear interaction between TRPC channels and spike-dependent calcium influx.

The necessity of TRPC channels for persistent spiking has been shown previously (e.g., by channel blockade with SKF-96365, interference at the C terminal domain with the peptide EQVTTRL, inhibition of upstream phospholipase C signaling with U73122; Zhang et al., 2011) and was verified in this study, but our demonstration that virtual CAN-like current causes persistent spiking (Fig. 6*B*) is the first direct experimental evidence for sufficiency. Furthermore, by combining dynamic clamp with calcium imaging, our data also show that virtual CAN-like current reproduces the calcium changes associated with persistent spiking, not by calcium influx through the virtual channel, but rather by activation of native VGCCs during spikes. This, together with evidence that L-type VGCCs are necessary for persistent spiking (see Introduction) whereas calcium release from intracellular stores is not (Egorov et al., 2006; Fransen et al., 2006; Zhang et al., 2011; Fig. 4*D*), argues that activation of TRPC channels relies on spike-dependent calcium influx. The apparent lack of calcium influx through TRPC channels is notable. Although homomeric TRPC5 channels are highly permeable to calcium (Okada et al., 1998), heteromeric channels that include TRPC1 subunits have reduced calcium permeability (Strübing et al., 2001; Storch et al., 2012). The specific subunit composition is also relevant for other aspects of channel activation (for review, see Reboreda et al., 2011; Freichel et al., 2014). Other channels such as TRPM4 have also been implicated in persistent spiking in PFC (Lei et al., 2014).

Despite including all of the biophysical details necessary for persistent spiking, we managed to keep our computational model simple enough that it could be studied thoroughly using bifurcation analysis. To compare our model with previous models of intrinsic bistability, one must consider the details of the persistent spiking modeled in each case carefully. Here, we will compare our model with that of Fransen et al. (2006), which focused on persistent spiking in entorhinal cortex (Egorov et al., 2002). The first difference is that persistent spiking in entorhinal cortex is graded, whereas persistent spiking in ACC is insensitive to the number or intensity of trigger stimuli. Second, depolarization lasting 0.5–4 s (and causing several evoked spikes) was required to trigger persistent spiking in entorhinal cortex, whereas we found that persistent spiking in ACC could be triggered by as few as one evoked spike. These two differences are important insofar as the trigger in the model by Fransen et al. (2006) is expected to cause a large calcium increase to a level much higher than maintained during persistent spiking in order to ratchet the fixed point attractor to a higher level. In our model, the threshold calcium level is lower than the steady-state calcium level associated with persistent

spiking. In fact, according to our model, the persistent spiking attractor sits much higher than threshold and specifically much higher above threshold than the quiescent attractor sits below threshold (Figs. 9 and 10 and experimental data in Fig. 7). The large separation in the former case explains the robustness of persistent spiking to distractors, whereas the small separation in the latter case explains the relative ease of triggering persistent spiking. The separation of two fixed point attractors by a saddle point and its associated separatrix (stable manifold) is a common dynamical basis for an on/off switch (Strogatz, 1998) and appears in other models of neuronal bistability (Loewenstein et al., 2005) even if the biophysical mechanisms are distinct from those described here.

However, whereas our fixed point attractors are static, the model proposed for persistent spiking in entorhinal cortex by Fransen et al. (2006) implemented a bistable switch to move the active attractor up or down based on external input causing a large increase or decrease in calcium that effectively increases or decreases the CAN current. In other words, the model by Fransen et al. (2006) included a switching mechanism (to move between attractors) and what we refer to here as a ratcheting mechanism (to reposition to active attractor). Ratcheting the fixed point attractor allows for graded persistent spiking that is more robust than is possible with a line attractor because the latter relies on several parameters to remain precisely balanced. Our proposed model does not include a ratcheting mechanism (because this was unnecessary to reproduce the nongraded persistent spiking observed in ACC neurons), but our simulations nonetheless show how varying $\bar{g}_{CAN}$ affects the steady-state firing rate (Fig. 8*D*) and the associated calcium level (Fig. 9*D*) for a given DC current. Dynamic regulation of $\bar{g}_{CAN}$ can be used to implement a ratcheting mechanism in our model, but the calcium thresholding proposed by Fransen et al. (2006) to ratchet $\bar{g}_{CAN}$ up or down (via a biochemical process such as phosphorylation/dephosphorylation) is incompatible with our calcium dynamics insofar as supramaximal calcium is necessary in our model for the robustness of persistent spiking and allowing supramaximal calcium to increase $\bar{g}_{CAN}$ would destabilize the system. Instead, we propose that intracellular calcium controls switching (as explained in Figs. 9, 10) and that PLC signaling (engaged by muscarinic, noradrenergic, and/or metabotropic glutamate receptors) works in parallel with control ratcheting, similar to what has been reported for M-type (KCNQ) channels (Kosenko et al., 2012) and TRPM5 channels (Liu and Liman, 2003). Given that persistent spiking in entorhinal cortex can also be enabled by metabotropic glutamate receptor activation (Yoshida et al., 2008), it would be interesting to test whether glutamate released from a persistently spiking neuron can act in an autocrine manner to regulate $\bar{g}_{CAN}$ through the parallel ratcheting mechanism we propose. The autocrine requirement is unnecessary if >1 neuron is considered and indeed cross-neuron metabotropic signaling could help coordinate $\bar{g}_{CAN}$ across persistently spiking neurons (Oikonomou et al., 2014). With respect to our proposed mechanism, it is notable that the capacity for graded persistent spiking washes out whereas nongraded persistent spiking is very robust (Reboreda et al., 2007), which suggests that the ratcheting mechanism involves diffusible messengers that are unnecessary for the switching mechanism.

To summarize, pyramidal neurons in ACC, like neurons in many other brain regions, can become intrinsically bistable under certain modulatory conditions. This bistability relies jointly on signaling triggered by metabotropic receptor activation and on spike-dependent calcium influx. Our results demonstrate the dynamical basis whereby spike-dependent calcium influx activates TRPC channels in a switch-like manner. The result is persistent spiking that is easily triggered yet is robust to distractors, and whose rate is insensitive to the triggers yet is sensitively modulated by ongoing input. These cellular mechanisms are likely to interact with network-level mechanisms to yield persistent spiking that can support working memory in ACC and many other areas of cortex.

References

Abel HJ, Lee JC, Callaway JC, Foehring RC (2004) Relationships between intracellular calcium and afterhyperpolarizations in neocortical pyramidal neurons. J Neurophysiol 91:324–335. CrossRef Medline

Adams SR, Kao JPY, Tsien RY (1989) Biologically useful chelators that take up Ca^{2+} upon illumination. J Am Chem Soc 111:7957–7968. CrossRef

Alfonso S, Benito O, Alicia S, Angélica Z, Patricia G, Diana K, Luis V (2008) Regulation of the cellular localization and function of human transient receptor potential channel 1 by other members of the TRPC family. Cell Calcium 43:375–387. CrossRef Medline

Berryman C, Stanton TR, Jane Bowering K, Tabor A, McFarlane A, Lorimer Moseley G (2013) Evidence for working memory deficits in chronic pain: a systematic review and meta-analysis. Pain 154:1181–1196. CrossRef Medline

Blair NT, Kaczmarek JS, Clapham DE (2009) Intracellular calcium strongly potentiates agonist-activated TRPC5 channels. J Gen Physiol 133:525–546. CrossRef Medline

Brody CD, Romo R, Kepecs A (2003) Basic mechanisms for graded persistent activity: discrete attractors, continuous attractors, and dynamic representations. Curr Opin Neurobiol 13:204–211. CrossRef Medline

Broersen LM, Heinsbroek RP, de Bruin JP, Uylings HB, Olivier B (1995) The role of the medial prefrontal cortex of rats in short-term memory functioning: further support for involvement of cholinergic, rather than dopaminergic mechanisms. Brain Res 674:221–229. CrossRef Medline

Durstewitz D, Seamans JK (2006) Beyond bistability: biophysics and temporal dynamics of working memory. Neuroscience 139:119–133. CrossRef Medline

Durstewitz D, Seamans JK, Sejnowski TJ (2000) Neurocomputational models of working memory. Nat Neurosci 3:1184–1191. CrossRef Medline

Egorov AV, Hamam BN, Fransen E, Hasselmo ME, Alonso AA (2002) Graded persistent activity in entorhinal cortex neurons. Nature 420:173–178. CrossRef Medline

Egorov AV, Unsicker K, von Bohlen und Halbach O (2006) Muscarinic control of graded persistent activity in lateral amygdala neurons. Eur J Neurosci 24:3183–3194. CrossRef Medline

El-Hassar L, Hagenston AM, D'Angelo LB, Yeckel MF (2011) Metabotropic glutamate receptors regulate hippocampal CA1 pyramidal neuron excitability via Ca^{2+} wave-dependent activation of SK and TRPC channels. J Physiol 589:3211–3229. CrossRef Medline

Ermentrout B (2002) Simulating, analyzing, and animating dynamical systems: a guide to XPPAUT for researchers and students. Philadelphia: SIAM.

Fransen E, Alonso AA, Hasselmo ME (2002) Simulations of the role of the muscarinic-activated calcium-sensitive nonspecific cation current INCM in entorhinal neuronal activity during delayed matching tasks. J Neurosci 22:1081–1097. Medline

Fransen E, Tahvildari B, Egorov AV, Hasselmo ME, Alonso AA (2006) Mechanism of graded persistent cellular activity of entorhinal cortex layer v neurons. Neuron 49:735–746. CrossRef Medline

Fraser DD, MacVicar BA (1996) Cholinergic-dependent plateau potential in hippocampal CA1 pyramidal neurons. J Neurosci 16:4113–4128. Medline

Freichel M, Tsvilovskyy V, Camacho-Londoño JE (2014) TRPC4- and TRPC4-containing channels. Handb Exp Pharmacol 222:85–128. CrossRef Medline

Fuster JM, Alexander GE (1971) Neuron activity related to short-term memory. Science 173:652–654. CrossRef Medline

Giovannini F, Knauer B, Yoshida M, Buhry L (2017) The CAN-in network: a biologically inspired model for self-sustained theta oscillations and memory maintenance in the hippocampus. Hippocampus 27:450–463. CrossRef Medline

Grienberger C, Konnerth A (2012) Imaging calcium in neurons. Neuron 73:862–885. CrossRef Medline

Gross SA, Guzmán GA, Wissenbach U, Philipp SE, Zhu MX, Bruns D, Cavalié A (2009) TRPC5 is a Ca^{2+}-activated channel functionally coupled to Ca^{2+}-selective ion channels. J Biol Chem 284:34423–34432. CrossRef Medline

Haj-Dahmane S, Andrade R (1996) Muscarinic activation of a voltage-dependent cation nonselective current in rat association cortex. J Neurosci 16:3848–3861. Medline

Haj-Dahmane S, Andrade R (1999) Muscarinic receptors regulate two different calcium-dependent non-selective cation currents in rat prefrontal cortex. Eur J Neurosci 11:1973–1980. CrossRef Medline

Hasselmo ME, Stern CE (2006) Mechanisms underlying working memory for novel information. Trends Cogn Sci 10:487–493. CrossRef Medline

Helmchen F, Imoto K, Sakmann B (1996) Ca^{2+} buffering and action potential-evoked Ca^{2+} signaling in dendrites of pyramidal neurons. Biophys J 70:1069–1081. CrossRef Medline

Jochems A, Yoshida M (2015) A robust in vivo-like persistent firing supported by a hybrid of intracellular and synaptic mechanisms. PLoS One 10:e0123799. CrossRef Medline

Knauer B, Jochems A, Valero-Aracama MJ, Yoshida M (2013) Long-lasting intrinsic persistent firing in rat CA1 pyramidal cells: a possible mechanism for active maintenance of memory. Hippocampus 23:820–831. CrossRef Medline

Kosenko A, Kang S, Smith IM, Greene DL, Langeberg LK, Scott JD, Hoshi N (2012) Coordinated signal integration at the M-type potassium channel upon muscarinic stimulation. EMBO J 31:3147–3156. CrossRef Medline

Lee JC, Callaway JC, Foehring RC (2005) Effects of temperature on calcium transients and Ca^{2+}-dependent afterhyperpolarizations in neocortical pyramidal neurons. J Neurophysiol 93:2012–2020. CrossRef Medline

Lei YT, Thuault SJ, Launay P, Margolskee RF, Kandel ER, Siegelbaum SA (2014) Differential contribution of TRPM4 and TRPM5 nonselective cation channels to the slow afterdepolarization in mouse prefrontal cortex neurons. Front Cell Neurosci 8:267. CrossRef Medline

Linley JE (2013) Perforated whole-cell patch-clamp recording. Methods Mol Biol 998:149–157. CrossRef Medline

Liu D, Liman ER (2003) Intracellular Ca^{2+} and the phospholipid PIP_2 regulate the taste transduction ion channel TRPM5. Proc Natl Acad Sci U S A 100:15160–15165. CrossRef Medline

Loewenstein Y, Mahon S, Chadderton P, Kitamura K, Sompolinsky H, Yarom Y, Häusser M (2005) Bistability of cerebellar purkinje cells modulated by sensory stimulation. Nat Neurosci 8:202–211. CrossRef Medline

Major AJ, Vijayraghavan S, Everling S (2015) Muscarinic attenuation of mnemonic rule representation in macaque dorsolateral prefrontal cortex during a pro- and anti-saccade task. J Neurosci 35:16064–16076. CrossRef Medline

Mori MX, Itsuki K, Hase H, Sawamura S, Kurokawa T, Mori Y, Inoue R (2015) Dynamics of receptor-operated Ca^{2+} currents through TRPC channels controlled via the $PI(4,5)P_2$-PLC signaling pathway. Front Pharmacol 6:22. CrossRef Medline

Navaroli VL, Zhao Y, Boguszewski P, Brown TH (2012) Muscarinic receptor activation enables persistent firing in pyramidal neurons from superficial layers of dorsal perirhinal cortex. Hippocampus 22:1392–1404. CrossRef Medline

Oikonomou KD, Singh MB, Sterjanaj EV, Antic SD (2014) Spiny neurons of amygdala, striatum, and cortex use dendritic plateau potentials to detect network UP states. Front Cell Neurosci 8:292. CrossRef Medline

Okada T, Shimizu S, Wakamori M, Maeda A, Kurosaki T, Takada N, Imoto K, Mori Y (1998) Molecular cloning and functional characterization of a novel receptor-activated TRP Ca^{2+} channel from mouse brain. J Biol Chem 273:10279–10287. CrossRef Medline

Prescott SA, Sejnowski TJ (2008) Spike-rate coding and spike-time coding are affected oppositely by different adaptation mechanisms. J Neurosci 28:13649–13661. CrossRef Medline

Prescott SA, Ratté S, De Koninck Y, Sejnowski TJ (2006) Nonlinear interaction between shunting and adaptation controls a switch between integration and coincidence detection in pyramidal neurons. J Neurosci 26:9084–9097. CrossRef Medline

Radzicki D, Pollema-Mays SL, Sanz-Clemente A, Martina M (2017) Loss of M1 receptor dependent cholinergic excitation contributes to mPFC deactivation in neuropathic pain. J Neurosci 37:2292–2304. CrossRef Medline

Rahman J, Berger T (2011) Persistent activity in layer 5 pyramidal neurons following cholinergic activation of mouse primary cortices. Eur J Neurosci 34:22–30. CrossRef Medline

Ratté S, Prescott SA (2011) ClC-2 channels regulate neuronal excitability, not intracellular chloride levels. J Neurosci 31:15838–15843. CrossRef Medline

Reboreda A, Raouf R, Alonso A, Séguéla P (2007) Development of cholinergic modulation and graded persistent activity in layer v of medial entorhinal cortex. J Neurophysiol 97:3937–3947. CrossRef Medline

Reboreda A, Jiménez-Díaz L, Navarro-López JD (2011) TRP channels and neural persistent activity. Adv Exp Med Biol 704:595–613. CrossRef Medline

Rubaiy HN, et al. (2017) Picomolar, selective, and subtype-specific small-molecule inhibition of TRPC1/4/5 channels. J Biol Chem 292:8158–8173. CrossRef Medline

Sidiropoulou K, Lu FM, Fowler MA, Xiao R, Phillips C, Ozkan ED, Zhu MX, White FJ, Cooper DC (2009) Dopamine modulates an mGluR5-mediated depolarization underlying prefrontal persistent activity. Nat Neurosci 12:190–199. CrossRef Medline

Storch U, Forst AL, Philipp M, Gudermann T, Mederos y Schnitzler M (2012) Transient receptor potential channel 1 (TRPC1) reduces calcium permeability in heteromeric channel complexes. J Biol Chem 287:3530–3540. CrossRef Medline

Strogatz SH (1998) Nonlinear dynamics and chaos: with applications to physics, biology, chemistry, and engineering. Don Mills, Ontario: Addison-Wesley.

Strübing C, Krapivinsky G, Krapivinsky L, Clapham DE (2001) TRPC1 and TRPC5 form a novel cation channel in mammalian brain. Neuron 29:645–655. CrossRef Medline

Tai C, Hines DJ, Choi HB, MacVicar BA (2011) Plasma membrane insertion of TRPC5 channels contributes to the cholinergic plateau potential in hippocampal CA1 pyramidal neurons. Hippocampus 21:958–967. CrossRef Medline

Vogt BA, Paxinos G (2014) Cytoarchitecture of mouse and rat cingulate cortex with human homologies. Brain Struct Funct 219:185–192. CrossRef Medline

von Bohlen Und Halbach O, Hinz U, Unsicker K, Egorov AV (2005) Distribution of TRPC1 and TRPC5 in medial temporal lobe structures of mice. Cell Tissue Res 322:201–206. CrossRef Medline

Yoshida M, Fransen E, Hasselmo ME (2008) mGluR-dependent persistent firing in entorhinal cortex layer III neurons. Eur J Neurosci 28:1116–1126. CrossRef Medline

Zhang Z, Séguéla P (2010) Metabotropic induction of persistent activity in layers II/III of anterior cingulate cortex. Cereb Cortex 20:2948–2957. CrossRef Medline

Zhang Z, Reboreda A, Alonso A, Barker PA, Séguéla P (2011) TRPC channels underlie cholinergic plateau potentials and persistent activity in entorhinal cortex. Hippocampus 21:386–397. CrossRef Medline

Zucker R (2010) Photorelease techniques for raising or lowering intracellular Ca^{2+}. Methods Cell Biol 99:27–66. CrossRef Medline

Zylberberg J, Strowbridge BW (2017) Mechanisms of persistent activity in cortical circuits: possible neural substrates for working memory. Annu Rev Neurosci 40:603–627. CrossRef Medline